Deep-Sea Research I 57 (2010) 1521–1531

Contents lists available at ScienceDirect

Deep-Sea Research I

journal homepage: www.elsevier.com/locate/dsri

Generation of internal waves by barotropic tidal flow over a steep ridge

Hui Qian [a], Ping-Tung Shaw [a,*], Dong Shan Ko [b]

[a] Department of Marine, Earth & Atmospheric Sciences, North Carolina State University, Raleigh, NC 27695-8208, USA
[b] Oceanography Division, Naval Research Laboratory, Stennis Space Center, MS 39529, USA

ARTICLE INFO

Article history:
Received 19 March 2010
Received in revised form
30 August 2010
Accepted 8 September 2010
Available online 16 September 2010

Keywords:
Internal wave generation
Barotropic tides
Ridges
Luzon Strait

ABSTRACT

A three-dimensional nonhydrostatic numerical model is used to study the generation of internal waves by the barotropic tidal flow over a steep two-dimensional ridge in an ocean with strong upper-ocean stratification. The process is examined by varying topographic width, amplitude of the barotropic tide, and stratification at three ridge heights. The results show that a large amount of energy is converted from the barotropic tide to the baroclinic wave when the slope parameter, defined as the ratio of the maximum ridge slope to the maximum wave slope, is greater than 1. The energy flux of internal waves can be normalized by the vertical integral of the buoyancy frequency over the ridge depths and the kinetic energy of the barotropic tides in the water column. A relationship between the normalized energy flux and the slope parameter is derived. The normalized energy flux reaches a constant value independent of the slope parameter when the slope parameter is greater than 1.5. It is inferred that internal wave generation is most efficient at the presence of strong upper-ocean stratification over a steep, tall ridge. In the Luzon Strait, the strength of the shallow thermocline and the location of the Kuroshio front could affect generation of internal solitary waves in the northern South China Sea.

1. Introduction

Large-amplitude internal waves are often observed in satellite remote sensing images in areas where the barotropic tides are forced to flow over a two-dimensional ocean ridge or the continental slope (Global Ocean Associates, 2004). Recent field observations have described the structure of internal waves in the northern South China Sea, (e.g., Ramp et al., 2004; Yang et al., 2004), Hawaiian Ridge (e.g., Nash et al., 2006), Bay of Biscay (e.g. Gerkema et al., 2004), and Massachusetts Bay (e.g. Scotti et al., 2007), to name a few. In the Luzon Strait, internal waves produced at the steep ridges evolve into large-amplitude internal solitary waves, propagating hundreds of kilometers westward into the northern South China Sea (Zhao and Alford, 2006; Chao et al., 2007). The flow velocity and thermocline depression could reach 2 m/s and 150 m, respectively (Ramp et al., 2004; Yang et al., 2004). In the deep ocean, the large vertical motion associated with internal waves is of concern to maritime activities. When propagating shoreward, breaking internal waves dissipate and lead to turbulent mixing (e.g., Moum et al., 2003), affecting plankton distribution, pollution, and sediment transport (Butman et al. 2006).

The baroclinic energy flux F associated with internal wave generation over a ridge is likely affected by the topographic width L, topographic height h_0, total water depth H, amplitude of tidal current U_0, forcing frequency ω, buoyancy frequency N, and the Coriolis parameter f. The nondimensional parameters associated with these quantities are reviewed by Garrett and Kunze (2007). An important parameter is the slope parameter γ, the ratio of the topographic slope to the slope of the internal wave beam $[(\omega^2-f^2)/(N^2-\omega^2)]^{1/2}$. A ridge is classified as supercritical if $\gamma>1$ and subcritical if $\gamma<1$. Other relevant parameters are the relative topographic height $\delta=h_0/H$, the local Froude number $F_r=U_0/(Nh_0)$, and the tidal excursion parameter $R_L=U_0/(\omega L)$.

Linear theory of internal wave generation is reviewed by Garrett and Kunze (2007). The solution in an ocean of infinite depth in the limit $\gamma\ll 1$ is given by Bell (1975). The infinite-depth solution establishes a scaling factor for the baroclinic energy flux

$$F\propto \rho_0 U_0^2 h_0^2 (N^2-\omega^2)^{1/2}(1-f^2/\omega^2)^{1/2}, \quad (1)$$

where ρ_0 is a reference density. The h_0^2 dependence for an isolated Gaussian bump has been confirmed by Balmforth et al. (2002). Eq. (1) has been used by nearly all theoretical studies on internal wave generation. In an ocean with depth-varying stratification, the linear theory of Llewellyn Smith and Young (2002) suggests that the buoyancy frequency at the ridge crest should be used for N in Eq. (1), and the wave slope is determined by a depth-averaged N using the WKB theory.

The energy flux in the solution of Bell (1975) is independent of the ridge slope (Llewellyn Smith and Young, 2002). The dependence of F on γ has been studied analytically by several

* Corresponding author. Tel.: +1 919 515 7276; fax: 1 919 515 7802.
E-mail address: pt_shaw@ncsu.edu (P.-T. Shaw).

0967-0637/$ - see front matter © 2010 Elsevier Ltd. All rights reserved.
doi:10.1016/j.dsr.2010.09.001

investigators. For an isolated Gaussian bump in an infinitely deep ocean, Balmforth et al. (2002) found that F is 14% above Bell's (1975) prediction as γ approaches 1. The prediction of Bell (1975) could be significantly reduced when the ocean is of finite depth (Llewellyn Smith and Young, 2002; Khatiwala, 2003). Of more interest is the range $\gamma>1$. In the extreme case of a knife-edge ridge ($\gamma\to\infty$) with small h_0, the energy flux is exactly twice that for a bell-shaped ridge with small slope (St Laurent et al., 2003; Llewellyn Smith and Young, 2003). Furthermore, the energy flux increases monotonically as the relative height δ increases and reaches two times Bell's (1975) prediction at $\delta=0.92$ (St Laurent et al., 2003; Llewellyn Smith and Young, 2003). Pétrélis, et al. (2006) showed that Bell's (1975) solution is a good prediction for subcritical ridges while the knife-edge solution provides a rough estimate for supercritical ridges.

At the critical slope, the solution is singular in the linear theory. Wave beams appear when γ approaches 1 (Balmforth et al., 2002; Khatiwala, 2003; Pétrélis et al., 2006) or when a knife-edge ridge is used (St Laurent et al., 2003; Llewellyn Smith and Young, 2003). In the nonlinear regime, Khatiwala (2003) found that energy flux of the internal wave may saturate for certain topographic shapes over a supercritical ridge. Transient hydraulic jumps over a supercritical ridge are demonstrated in the nonhydrostatic numerical simulation of Legg and Klymak (2008). This overturning process may saturate the energy flux of large-amplitude internal waves over a supercritical ridge, making the energy flux less dependent on the slope parameter.

The effect of $R_L>1$ is known to generate internal waves of higher tidal harmonics both analytically (Bell, 1975) and numerically (Legg and Huijts, 2006). In the Luzon Strait, typical amplitude of the barotropic tidal current is 0.1 m/s, and the excursion parameter R_L is much less than one. Thus, energy of internal waves in the Luzon Strait occurs mostly at tidal frequencies. The Froude number is small over the tall ridges reaching the thermocline in the Luzon Strait. Nonlinearity in the Luzon Strait is mainly due to large topographic slope and the large ratio of the ridge height to water depth δ. In this study, nonhydrostatic simulation is performed to investigate the mechanisms of internal wave generation over a tall, steep ridge in an ocean with strong stratification in the upper ocean. The internal wave energy flux is calculated to find its dependence on γ at different ridge heights.

The paper is organized as follows. Section 2 describes the model setup. The model results are presented in Section 3 for three sets of experiments at different ridge heights. Effects of the topographic width, barotropic tidal amplitude, and stratification on the internal wave energy flux are studied in each set of experiments. A parameterization scheme for energy flux is derived and compared with order-of-magnitude estimation from the real ocean in Section 4, followed by discussion and conclusion.

2. Model description and experiments

The numerical experiments in this paper extend the study of Shaw et al. (2009) in the parameter space. The three-dimensional nonhydrostatic numerical model of Shaw and Chao (2006) is used. The model solves the three-dimensional momentum, continuity, and density equations with Boussinesq and rigid-lid approximations. The governing equations are

$$\frac{D\mathbf{u}}{Dt}+2\Omega\mathbf{k}'\times\mathbf{u}=-\frac{1}{\rho_0}\nabla p-\frac{\rho}{\rho_0}g\mathbf{k}+A_H\nabla_H^2\mathbf{u}+\nu\frac{\partial^2\mathbf{u}}{\partial z^2} \tag{2}$$

$$\nabla\cdot\mathbf{u}=0. \tag{3}$$

$$\frac{D\rho}{Dt}=K_H\nabla_H^2\rho+\kappa\frac{\partial^2\rho}{\partial z^2}. \tag{4}$$

where $\mathbf{u}$ is the three-dimensional velocity vector (u, v, w) in the (x, y, z) coordinates, $\mathbf{k}'$ is a unit vector pointing upward from the North Pole, $\mathbf{k}$ is the local upward unit vector, ρ is the deviation of density from a reference density ρ_0(1028 kg m^{-3}), Ω is the Earth's rotation rate, and p is the pressure. The kinematic eddy viscosity and diffusivity are constant, so that $A_H=10^6$ m^2 s^{-1}, $K_H=10^5$ m^2 s^{-1}, $\nu=1\times10^{-4}$ m^2 s^{-1}, and $\kappa=0.1\times10^{-4}$ m^2 s^{-1}. Eq. (2) includes both the horizontal and vertical components of the Coriolis acceleration. The finite difference form of the governing equations and the solution procedure are described in Shaw and Chao (2006).

The model domain is from $x=-200$ to 200 km in the east-west direction and from $z=-H=-800$ m at the bottom to 0 m at the surface. The latitude of the Luzon Strait (20°N) is used in calculating the Coriolis parameter. The horizontal and vertical grid sizes are 200 and 10 m. In the y direction, two grid cells are used. With a periodic boundary condition, no y-variation is introduced if the initial values are independent of y. In effect, the three-dimensional model performs a two-dimensional simulation in this study. At $x=0$ is a bell-shaped (Witch-of-Agnesi) ridge

$$h(x)=h_m/[1+(x/L)^2] \tag{5}$$

where h_m is the maximum height and L is the half-width of the ridge. The maximum ridge slope, located at $x=3^{1/2}L$, is $(3^{3/2}/8)h_m/L$. In this study, h_m is fixed at 600 m, and L is varied to change the maximum slope. Without affecting the maximum slope, the ridge is displaced vertically to alter the ridge height h_0, which is measured from the bottom ($z=-800$ m) to the ridge crest.

Flow over the ridge is forced by the oscillating barotropic M_2 tide. The velocity in the x-direction is given by

$$U=U_0\sin(\omega t), \tag{6}$$

where $\omega=1/12.42\,\mathrm{h}^{-1}=1.41\times10^{-4}\,\mathrm{s}^{-1}$ is the tidal frequency. The barotropic tidal current is 0 at $t=0$ and becomes positive in the first half tidal cycle. In this paper, positive tidal velocity is called ebb tide as in the Luzon Strait.

The perturbation density ρ' is

$$\rho'(x,z,t)=\rho-\rho_a(z). \tag{7}$$

The ambient stratification $\rho_a(z)$ is given by

$$\rho_a(z)=-\frac{\Delta\rho}{2}\left[1+\tanh\left(\frac{z-z_0}{D}\right)\right]. \tag{8}$$

where $\Delta\rho$ is the scale of density perturbation. The thermocline is centered at depth z_0 ($=-50$ m) with thickness D ($=120$ m). The buoyancy frequency derived from Eq. (8) is

$$N=[-(g/\rho_0)d\rho_a/dz]^{1/2}=\left(\frac{g\Delta\rho}{2\rho_0 D}\right)^{1/2}\mathrm{sech}\left(\frac{z-z_0}{D}\right)=N_{\max}\mathrm{sech}\left(\frac{z-z_0}{D}\right). \tag{9}$$

The maximum buoyancy frequency $N_{\max}$ is located at $z=z_0$. For $\Delta\rho=6\,\mathrm{kg}/m^3$ and $\rho_0=1028\,\mathrm{kg}/m^3$, $N_{\max}=N_0=0.015\,\mathrm{rad}/s$. Mode-1 waves associated with Eq. (9) have zero horizontal velocity and maximum vertical velocity at $z=-200$ m (see Fig. 1 in Shaw et al., 2009). The phase speed of the mode-1 wave is 1.52 m/s for $N_{\max}=N_0$, and is proportional to $N_{\max}$ in other experiments. For semidiurnal tides, the internal wave is evanescent below $z=-700$ m.

The baroclinic velocity $\mathbf{u}'\equiv(u',v',w')$ is calculated by subtracting the depth-averaged horizontal velocity from the total velocity $\mathbf{u}$. The perturbation kinetic energy density is defined by

$$K=\frac{1}{2}\rho_0(u'^2+v'^2+w'^2), \tag{10}$$

and the perturbation potential energy density is

$$P = \frac{1}{2}\frac{g^2\rho'^2}{\rho_0 N^2}. \quad (11)$$

The internal wave energy density E is the sum of Eqs. (10) and (11).

The internal wave energy flux is $p'\mathbf{u}'$, where p' is the perturbation pressure. The perturbation pressure p' is obtained by subtracting the depth-averaged hydrostatic pressure $\overline{p}$ from p (Nash et al., 2005):

$$p'(x,z,t) = p(x,z,t) - \overline{p}(x,t). \quad (12)$$

The depth averaged pressure is given by

$$\overline{p} = \frac{1}{|z_b|}\int_{z_b}^{0} dz\left(\int_{z}^{0}\rho'(x,z',t)g dz'\right) \quad (13)$$

where z_b is the z-coordinate of the bottom. In this paper, the sum of the maximum horizontal energy flux on the two sides of the ridge at $x=-x_B$ and x_B represents the total internal wave energy produced by the ridge

$$F = -\int_{z_b}^{0} p'u'|_{x=x_B}dz + \int_{z_b}^{0} p'u'|_{x=-x_B}dz. \quad (14)$$

Table 1
List of experiments. Each experiment is carried out for ridge heights $h_0=200$, 400, and 600 m.

Experiments	L (km)	U_0 (m/s)	N_{max}
1a	15	0.1	N_0
1b	30	0.1	N_0
1c	45	0.1	N_0
1d	60	0.1	N_0
2a	30	0.05	N_0
2b	30	0.2	N_0
3a	30	0.1	$N_0/2$
3b	30	0.1	$2^{1/2}N_0$
4a	15	0.1	$N_0/2$
4b	15	0.1	$2^{1/2}N_0$

3. Results

Three sets of experiments with $h_0=200$, 400, and 600 m are carried out in this study. Table 1 lists the topographic width L, the amplitude of the barotropic tidal velocity U_0, and the maximum buoyancy frequency N_{max} for each h_0.

3.1. Internal wave generation

Fig. 1 shows the distribution of the baroclinic velocity u' during the ebb phase of the fourth tidal cycle in experiment 1a with $h_0=400$ m. The barotropic tidal current is zero in the top and bottom panels and eastward in the two middle panels. In Fig. 1, waves emit from the ridge crest and split into two nearly symmetric paths in the strongly stratified upper ocean. Over the ridge, the baroclinic velocity u' is initially negative and becomes positive following the development of the positive barotropic tidal current. Thus, a wave beam of positive (negative) u' over the ridge top originates at the beginning of the ebb (flood) tide (Shaw et al., 2009).

Downward wave reflections by the surface occur at $x=\pm 26$ and ± 75 km. At $x=\pm 50$ km, waves are reflected upward from $z=-200$ m, the lower boundary of the thermocline. Mode-1 waves appear beyond $x=\pm 100$ km. Intensification of the wave front with negative u' leads to a tidal bore at $x=-120$ km in Fig. 1a. This bore can be traced back to the start of the flood tide in the second tidal cycle. Tidal bores with positive u' form on the east side of the ridge. These tidal bores eventually develop into rank-ordered internal solitary waves (Shaw et al., 2009).

Internal wave energy density at $z=-5$ m for experiment 1a is shown on the x–t plane in Fig. 2. Maxima are at $x=\pm 26$ and ± 75 km, locations of the first and second wave reflections from the surface in Fig. 1. Propagation of mode-1 hydrostatic waves is shown as bands of energy maxima on each side of the ridge. The stronger ones are associated with negative (positive) u' on the left- (right-)hand side of the ridge in Fig. 1a. The speed of propagation is close to the mode-1 phase velocity of 1.52 m/s. The energy density of the mode-1 wave is nearly uniform during propagation. Small-scale solitary waves are shown as strings of localized maxima; the data used for plotting are stored hourly, insufficient to resolve the propagation of short waves (Shaw et al., 2009).

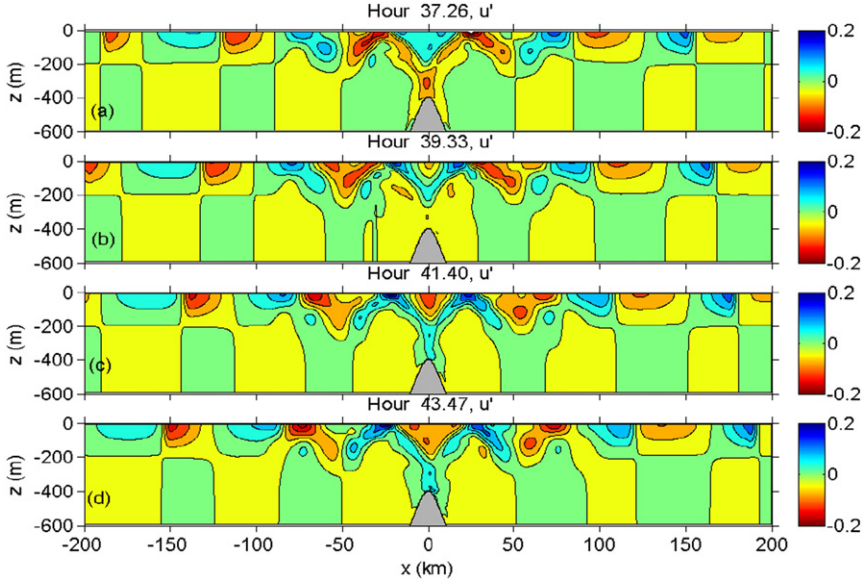

Fig. 1. Contour plots of the baroclinic velocity u' (m/s) in experiment 1a with $L=15$ km and $h_0=400$ m at $t=37.26$ to 43.47 h with time increments of 2 h. The barotropic tidal flow is to the right in the two middle panels. The contour interval is 0.04 m/s.

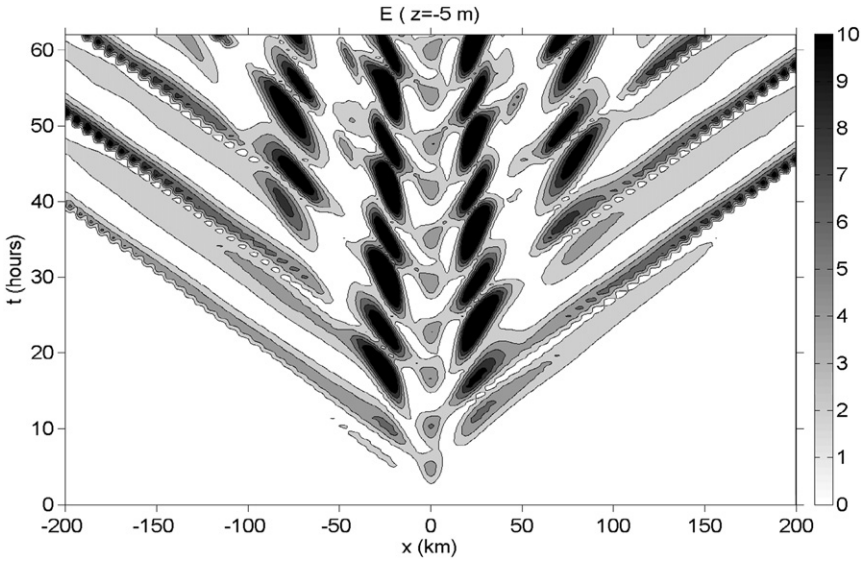

Fig. 2. Contour plot of internal wave energy density (J/m^3) at $z=-5$ m on the x–t plane for experiment 1a. The contour interval is 2 J/m^3.

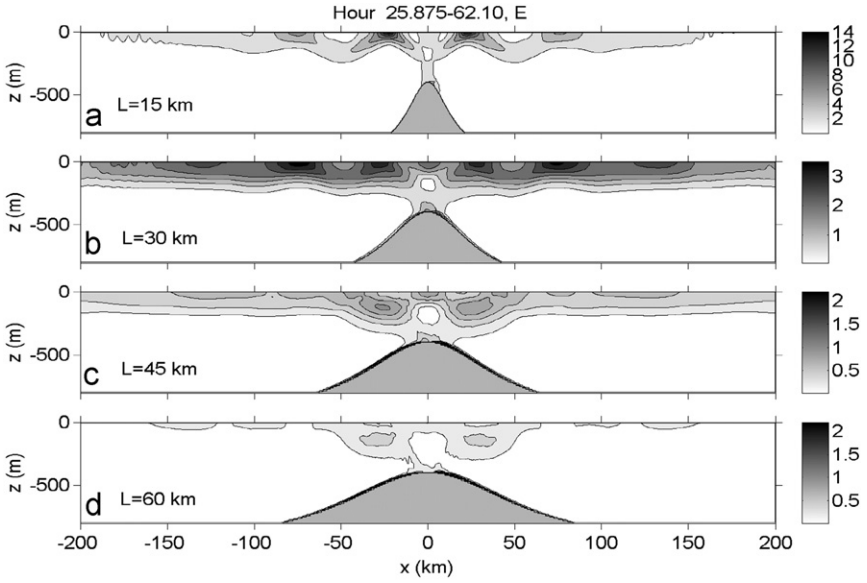

Fig. 3. Internal wave energy density (J/m^3) for L equal to (a) 15, (b) 30, (c) 45, and (d) 60 km (experiments 1a–d) with ridge height at 400 m. Averaging is performed on hourly data over three tidal cycles between $t=25.88$ and 62.10 h. The contour intervals in the four panels are 2, 0.5, 0.2, and 0.2 J/m^3, respectively.

3.2. *Effects of topographic width*

Fig. 3 compares the internal wave energy density for ridges of four different widths (experiments 1a–d) with the same ridge height $h_0=400$ m. The energy density is the average of the hourly data over 3 tidal cycles from 25.875 to 62.1 h. Fig. 3a shows the result from experiment 1a with the steepest ridge slope ($L=15$ km). Internal wave beams similar to those in the u' plot in Fig. 1 are clearly seen. Between 200 and 400 m depths, wave beams are nearly vertical because of the weak stratification in the water column. In the strongly stratified upper 200 m of the water column, wave beams are refracted toward the horizontal direction. Symmetric wave beams appear on the two sides of the ridge. Wave reflections from the surface occur near the edge of topographic influence and produce energy density maxima at the surface. After reflection, internal waves propagate away from the ridge in an upper ocean wave guide.

Increasing L to 30 km reduces the energy density and widens the wave beam (Fig. 3b). Internal wave beams are barely visible, but maxima in energy density are still at the surface. At $L=45$ and 60 km, distribution of the energy density differs greatly from that for a narrow ridge (Fig. 3c,d). The maximum energy density is much smaller than that in Fig. 3a. Furthermore, reflections from the surface produce maxima at $z=-125$ m instead of the surface. Fig. 3 suggests that the ridge with $L=15$ km is supercritical, and the ridges with $L=45$ and 60 km are subcritical. The slope is near the critical value for the ridge with $L=30$ km. A supercritical ridge is most efficient in producing internal waves.

The vertical energy flux $w'p'$ at $t=41.40$ h is shown in Fig. 4 for experiments 1a and 1d with $L=15$ and 60 km, respectively. Over a narrow ridge (Fig. 4a), energy flux between $z=-700$ and -200 m is large and upward on the flank of the ridge. Above $z=-200$ m, upward and downward fluxes follow the path of the wave beam shown in Fig. 3a. Free propagating hydrostatic waves occur at

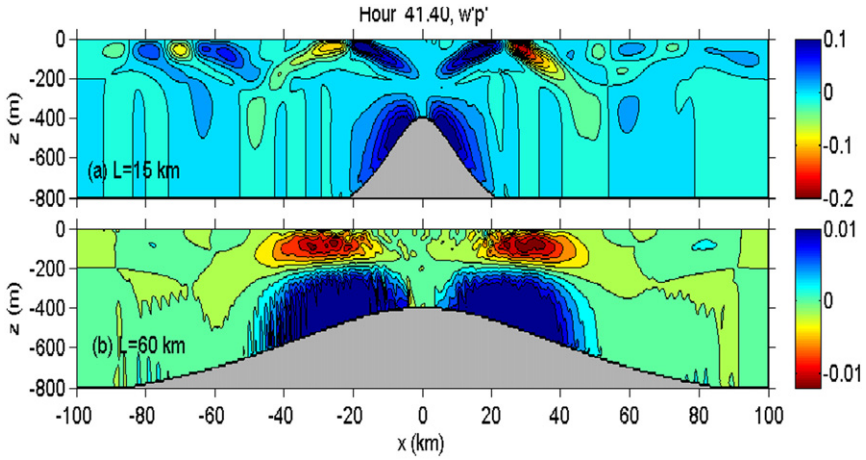

Fig. 4. Distribution of the vertical energy flux (W/m^2) at 41.40 h in experiments (a) 1a and (b) 1d with ridge height at 400 m. The contour intervals are 0.02 and 0.002 W/m^2, respectively.

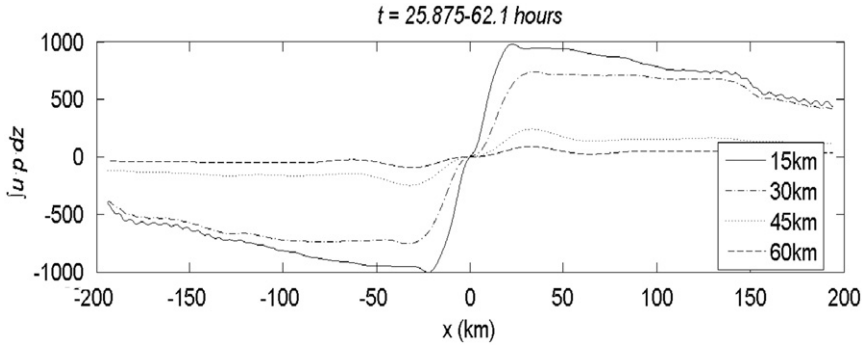

Fig. 5. Vertically integrated horizontal energy flux (W/m) as a function of x for $L=15$, 30, 45, and 60 km with ridge height at 400 m (experiments 1a–d). The flux is averaged over three tidal cycles from 25.88 to 62.1 h. The ridge is located at $x=0$ km.

$|x|>60$ km. When $L=60$ km (Fig. 4b), energy flux is mainly over the flank of the ridge, upward below $z=-200$ m and downward in the upper 200 m similar to a mode-1 standing wave. The flux is nearly 10 times smaller than in experiment 1a, and little energy leaves the ridge topography.

Fig. 5 shows the distribution of vertically integrated horizontal energy flux $\int_{z_b}^{0} u'p'dz$ as a function of x in experiments 1a–1d. The flux is averaged over 3 tidal periods as in Fig. 3. The horizontal energy fluxes increase rapidly with x near the ridge crest, reach maximum values at the location of maximum energy density at the surface, and decay slightly thereafter (Fig. 3). The maximum horizontal energy flux is highest in experiments using the narrowest ridge ($L=15$ km) and decreases rapidly with increasing ridge width. The ridge half-width gives the proper horizontal length scale in this plot.

3.3. Effects of the barotropic tidal current

Fig. 6 compares the internal wave energy density generated by barotropic tidal currents of amplitudes $U_0=0.2$, 0.1, and 0.05 m/s over a 400-m ridge with $L=30$ km. The pattern of internal wave energy density is qualitatively similar in the three experiments; only the magnitudes are different. Ripples in the experiment of the strongest tidal current indicate the formation of internal solitary waves (Fig. 2).

Fig. 7 shows the vertically integrated horizontal energy flux normalized by U_0^2 for the three experiments plotted in Fig. 6. After normalization, the three curves become similar, especially in the wave generation region. Fig. 7 confirms that the internal wave energy flux is proportional to the square of the amplitude of the barotropic tidal current as suggested in the linear theory. In the range of parameters used in this study, varying the strength of the barotropic tidal current does not affect the generation of internal waves qualitatively.

3.4. Effects of stratification

The perturbation density fields at 37.26 h in experiments 3b and 3a with $N_{max}=2^{1/2}N_0$ and $N_0/2$, respectively, are shown in Fig. 8. The ridge height h_0 is 400 m and $L=30$ km. When $N_{max}=2^{1/2}N_0$, wave beams form over the ridge crest (Fig. 8a). The angle of the wave beam with the vertical is greater than that at $N_{max}=N_0$ in Fig. 4a, consistent with the internal wave theory. Large-amplitude internal waves of wavelength greater than the scale of topography propagate away from the ridge. In weak stratification (Fig. 8b), internal waves generated over the ridge are weak and form a mode-1 standing wave over the ridge topography. Patterns of the vertical energy flux in experiments 3b and 3a are similar to those in Fig. 4 (not shown).

Fig. 9 shows the average energy density of internal waves in experiments 3b, 1b, and 3a with maximum buoyancy frequency $N_{max}=2^{1/2}N_0$, N_0, and $N_0/2$, respectively. The ridge height h_0 is 400 m and $L=30$ km. The distribution of energy density differs qualitatively in these experiments. As shown in Fig. 3b, the ridge slope in experiment 1b is near the critical value (Fig. 9b). When $N_{max}=2^{1/2}N_0$, vertically propagating wave beams in the upper ocean are distinct (Fig. 9a). On the other hand, standing waves form over the ridge for $N_{max}=N_0/2$ (Fig. 9c), similar to the

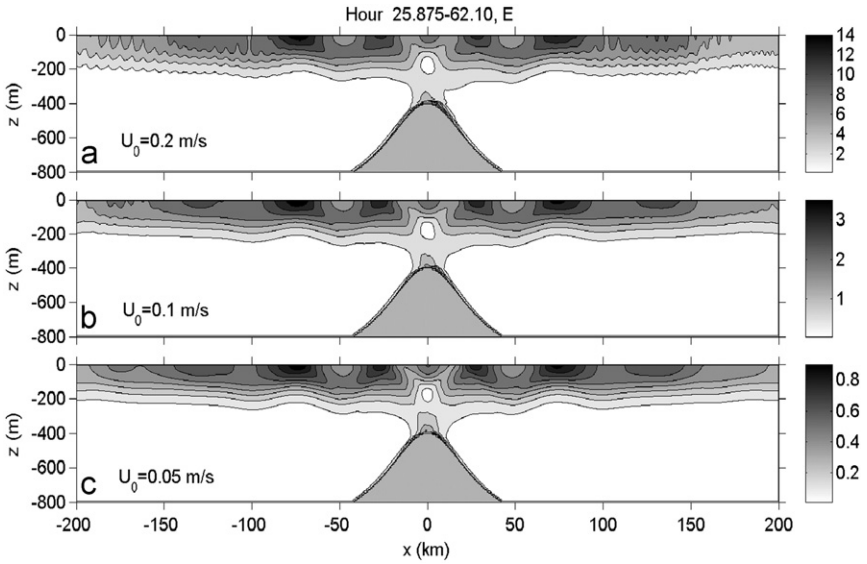

Fig. 6. Distribution of internal wave energy density (J/m^3) for U_0 equal to (a) 0.2, (b) 0.1, and (c) 0.05 m/s with h_0=400 m and L=30 km (experiments 2b, 1b, and 2a). The energy density is averaged from 25.88 to 62.1 h. The contour intervals are 2, 0.5, and 0.1 J/m^3, respectively.

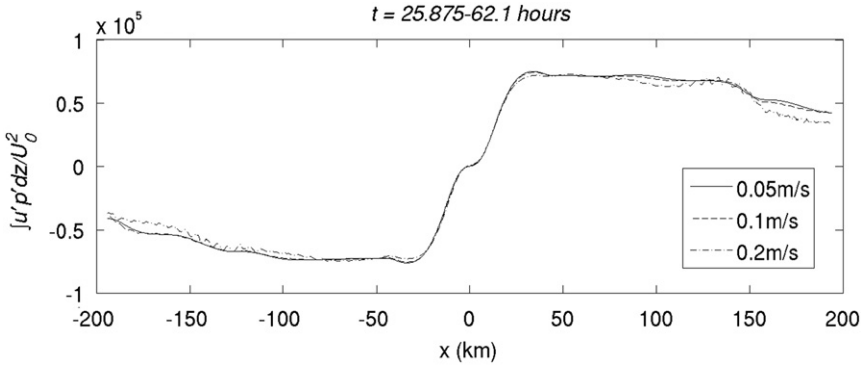

Fig. 7. Vertically integrated horizontal energy flux (W/m) as a function of x for the three experiments shown in Fig. 6. The energy flux is normalized by U_0^2 and averaged over three tidal cycles from 25.88 to 62.1 h.

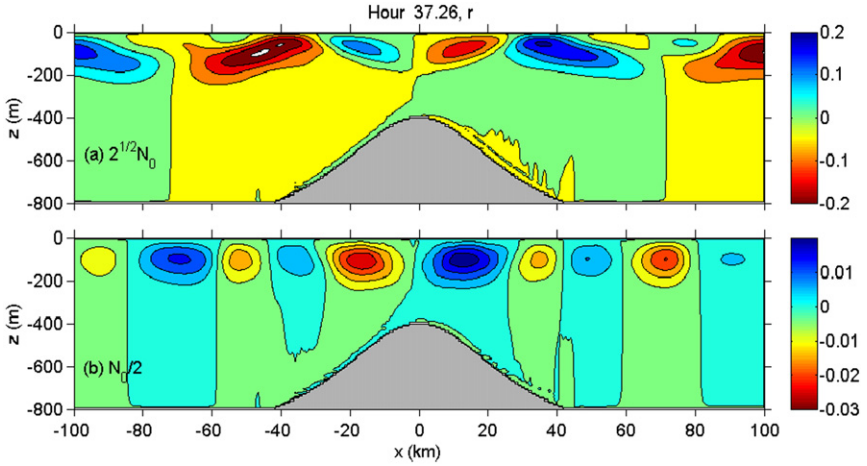

Fig. 8. Distribution of density perturbation ρ' (kg/m^3) at t=37.26 h for experiments (a) 3b and (b) 3a, with contour intervals at 0.05 and 0.005 kg/m^3, respectively.

experiment with L=60 km in Fig. 3d. The maxima in energy density in Fig. 9c are located below surface. The energy flux of the internal wave is largest in Fig. 9a. Increasing stratification has the same effect on internal wave generation as increasing the ridge slope. When stratification is strong, wave beams form and a large amount of internal wave energy radiates away from the ridge.

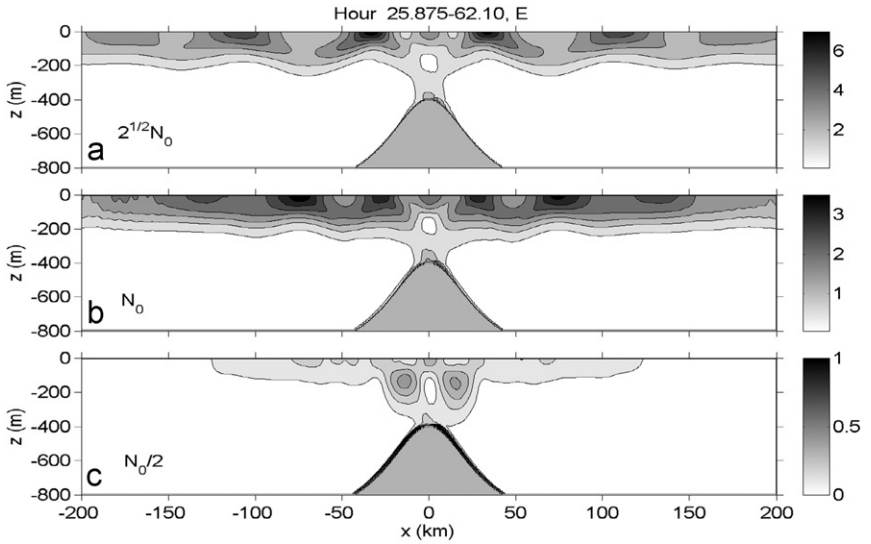

Fig. 9. Distribution of internal wave energy density (J/m^3) for ridges at $h_0=400$ m and $L=30$ km in experiments (a) 3b, (b) 1b and (c) 3a. Time average is over the same period as in Fig. 3. The contour intervals are 1, 0.5, and 0.1 J/m^3, respectively.

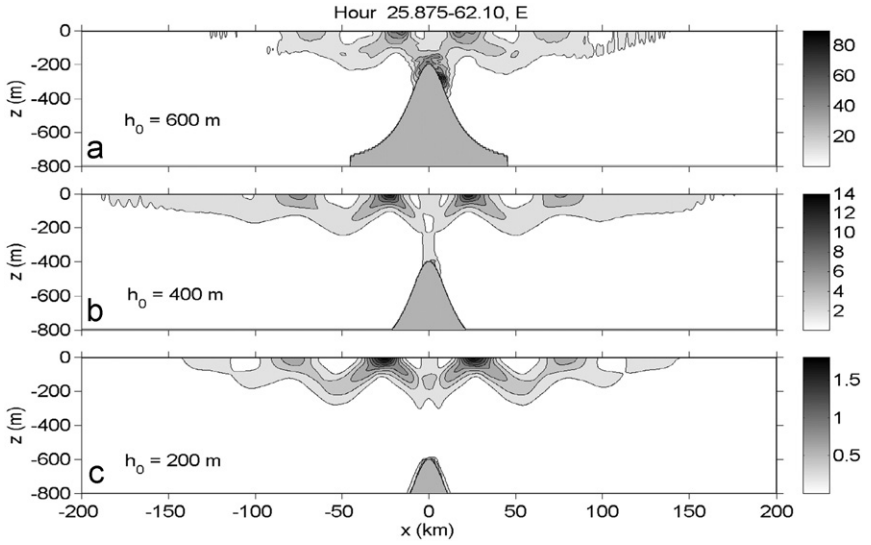

Fig. 10. Distribution of internal wave energy density (J/m^3) for varying ridge heights at $L=15$ km. The energy density is averaged over three tidal cycles from 25.88 to 62.1 h. The contour intervals are 10, 2, and 0.2 J/m^3, respectively.

3.5. *Effects of ridge height*

Fig. 10 shows the energy density of the internal wave for a steep ridge with $L=15$ km at $h_0=200$, 400, and 600 m. The parameters are the same as those in experiment 1a. The wave patterns in these experiments are similar. Above $z=-200$ m, wave beams form at nearly the same locations in all three experiments. However, the maximum energy is much reduced when the ridge height decreases. The ratio of energy density from the smallest ridge to the tallest ridge is 1:7.5:30.

Varying the ridge height h_0 in experiment 1d ($L=60$ km) does not change the pattern of the internal wave; subsurface maxima appear over the ridge in all experiments (Fig. 11). Similar to the experiments with a narrow ridge in Fig. 10, maximum energy density decreases rapidly with decreasing ridge height. The energy ratio for the three ridges is 1:2:20. In the linear theory (Llewellyn Smith and Young, 2002), the ratio is 1:5:24, the buoyancy frequency ratio at the depth of the ridge crest. The energy ratios in the numerical experiments have the same order of magnitude as that obtained from the linear theory but the linear theory underestimates (overestimates) the energy density of the internal wave when the topographic slope is supercritical (subcritical).

4. Parameterization of the energy flux

Experiments using parameters shown in Table 1 are repeated for three ridge heights $h_0=200$, 400, and 600 m. From these experiments, a parameterization scheme can be formulated to describe the dependence of the vertically integrated horizontal energy flux on the ridge slope, barotropic tidal current amplitude, and stratification for each topographic height. Normalization of the energy flux based on the linear theory is modified to fit the numerical data for tall ridges. The scheme is represented by a nondimensional relationship between the normalized energy flux and the slope parameter γ.

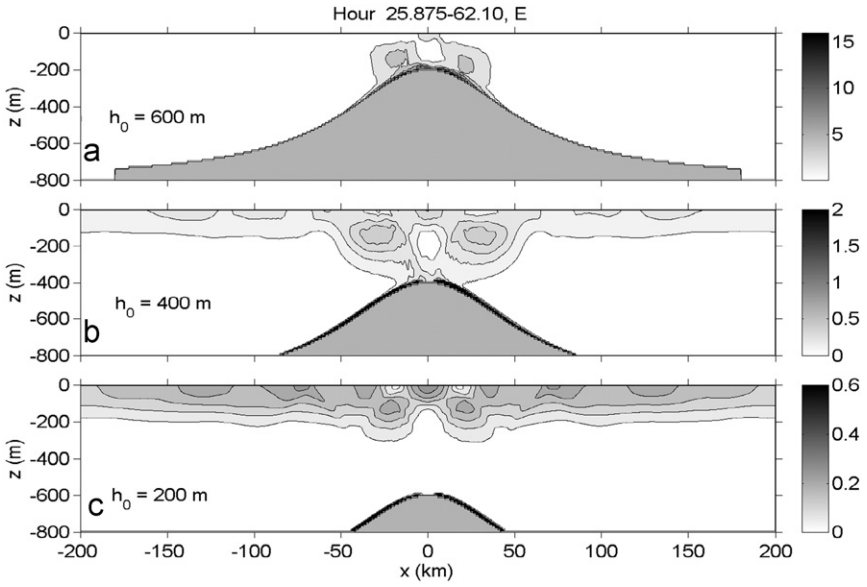

Fig. 11. Same as Fig. 10 except for $L=60$ km. The contour intervals are 2, 0.1, and 0.05 J/m^3, respectively.

4.1. Normalization scheme

The experiments in Section 3.3 show that U_0^2 is an appropriate factor for energy flux generated over finite ridges. Physically, the energy flux should be proportional to the depth-integrated barotropic tidal energy. Thus, it is reasonable to scale the energy flux by HU_0^2. In the linear theory, the buoyancy frequency at the ridge crest provides another scaling factor. However, Fig. 4 shows that the vertical energy flux is affected by a large area of the ridge flank, not just the ridge crest. A better scale would be the averaged buoyancy frequency over the depths of the ridge

$$\overline{N}_r = \frac{1}{h_0}\int_{-H}^{-H+h_0} N dz. \tag{15}$$

Using Eq. (15), the local Froude number becomes

$$F_r = \frac{U_0}{\overline{N}_r h_0}. \tag{16}$$

The normalized energy flux is defined as

$$F' = \frac{F}{\rho H {U_0}^2 \overline{N}_r h_0}. \tag{17}$$

If multiplied by δ, the normalization factor in Eq. (17) is the same as that of Eq. (1) for $N \gg \omega$ and $f=0$ in an ocean of constant stratification.

The slope parameter γ depends on the ridge slope and the slope of the wave beam; both are not constant in this study. In Section 3.5, raising or lowering the ridge affects the energy density of the internal wave but not the wave beam in the upper 200 m of the water column (Figs. 10 and 11). Therefore, the maximum ridge slope, which does not vary in these experiments, is a good description of γ. Furthermore, Fig. 4a shows that tilting of the wave beam in the strongly stratified upper-ocean wave guide could be represented by the averaged wave slope between $z_t=-200$ m and 0 m

$$s = \frac{1}{|z_t|}\int_{z_t}^{0}\left(\frac{\omega^2-f^2}{N^2-\omega^2}\right)^{1/2} dz. \tag{18}$$

Table 2
The nondimensional horizontal energy flux (F'), the slope parameter (γ), and the local Froude number (F_r) calculated from all experiments in this study.

Ridge height (h_0)	600 m			400 m			200 m		
experiment	F'	γ	F_r	F'	γ	F_r	F'	γ	F_r
1a	1.16	2.6	0.1	1.35	2.6	0.56	0.62	2.6	2.5
1b	0.81	1.3	0.1	1.01	1.3	0.56	0.81	1.3	2.5
1c	0.30	0.87	0.1	0.33	0.87	0.56	0.74	0.87	2.5
1d	0.06	0.65	0.1	0.12	0.65	0.56	0.35	0.65	2.5
2a	0.84	1.3	0.05	1.02	1.3	0.28	0.81	1.3	1.25
2b	0.74	1.3	0.2	0.96	1.3	1.11	0.80	1.3	5
3a	0.05	0.65	0.2	0.12	0.65	1.19	0.32	0.65	5
3b	1.08	1.83	0.07	1.24	1.83	0.37	0.80	1.83	2
4a	0.70	1.3	0.2	1.07	1.3	1.19	0.83	1.3	5
4b	1.40	3.67	0.07	1.12	3.67	0.37	0.58	3.67	2

The slope parameter γ is the ratio of the maximum topographic slope and s.

Table 2 summarizes the nondimensional parameters obtained from all experiments in this study. The Froude number is less than 1.2 for $h_0=400$ and 600 m and is greater than 1.2 for $h_0=200$ m. The normalized horizontal energy flux F' is plotted in Fig. 12 for these two groups. Two curves are drawn to describe the dependence of F' on γ. In Fig. 12a, F' is nearly constant for large γ and decreases to zero rapidly at $\gamma<1$. The transition occurs between $\gamma=0.5$ and 1.5. It seems that energy conversion by wave beams is possible only when the ridge slope is supercritical. Similarly, the normalized energy flux in Fig. 12b is nearly zero for subcritical ridges as in Fig. 12a. In the supercritical range, F' decreases slightly with increasing γ. Fig. 12 suggests that barotropic-to-baroclinic energy conversion occurs only when γ is greater than 1.

4.2. Comparison with observations

Table 3 lists the energy fluxes of strong internal waves at four locations in the world ocean from earlier observations and numerical studies. The energy flux in the Luzon Strait is from the real-time simulation at Naval Research Laboratory for 2005 (S. F. Lin, 2009, personal communication). At French Frigate, the maximum internal wave energy flux is 39 kW/m from velocity

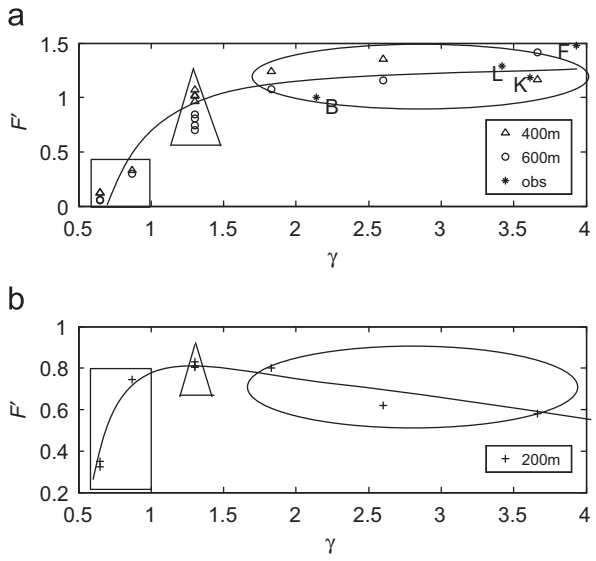

Fig. 12. Plots of normalized horizontal energy flux (F') in Table 2 as a function of the slope parameter (γ): (a) for ridge heights at 400 m (triangles) and 600 m (circles) and (b) for ridge heights at 200 m (crosses). In the top panel, ∗ represents estimates in the ocean at Bay of Biscay (B), Luzon Strait (L), French Frigate (F) and Kauai Channel (K) from Table 3. The three regimes for small, near critical, and large γ are enclosed by a rectangle, triangle, and ellipse, respectively.

Table 3
Energy fluxes (F), depth range of ridges, the slope parameter (γ), and the amplitude of barotropic tidal current (U_0) at locations where strong internal waves are observed.

Location	F (kW/m)	Depth range (m)	γ	U_0 (m/s)
Luzon Strait	55	500–3000	3.42	0.06
French Frigate	40	900–3400	3.93	0.05
Kauai Channel	26	1000–3000	3.61	0.05
Bay of Biscay	10	250–4000	2.14	0.025

measurements (Rudnick et al., 2003) and 45 kW/m from internal tide simulation (Simmons et al., 2004). The averaged value is included in Table 3. The energy flux in Kauai Channel is from the estimate of Simmons et al. (2004). The energy flux at Bay of Biscay is from the current meter measurements of Gerkema et al. (2004).

The bottom depth is obtained from the Gridded Global Relief Data (ETOPO2) with 2-min resolution (http://www.ngdc.noaa.gov/mgg/fliers/01mgg04.html). Topography is smoothed by a 2-D Savitzky-Golay filter (Ratzlaff and Johnson, 1989; Kuo et al., 1991). The topographic slope is then calculated from the smoothed topography as the first derivatives with respect to x and y. The buoyancy frequency is calculated from the climatological temperature and salinity fields of Levitus (1998, http://www.esrl.noaa.gov/psd/data/gridded/data.nodc.woa98.html). The amplitude of the barotropic tidal current is obtained from previous studies (e.g. Legg and Klymak, 2008; Gerkema et al., 2004; Jan et al., 2008).

The depth range of the ridge is obtained from the smoothed topography. The ridge slope is the average topographic slope in this range. The wave slope is estimated using Eq. (18). Large uncertainties exist in the calculation of maximum topographic slope and thusγ. Nevertheless, the estimated γ is greater than 1 at all four locations. The vertical integral of the buoyancy frequency in the depth range of the ridge is obtained from Eq. (15) for normalization of the energy flux and calculation of the local Froude number (16). The Froude number is much smaller than 1 at all locations. The normalized energy fluxes are nearly constant for the four locations and follow the curve in Fig. 12a.

5. Discussion

In this study, the wave beam is nearly vertical below 200 m because of weak stratification in the deep water. The slope parameter γ for the supercritical ridges at 200 and 400 m would be much smaller than 1 if calculated from the depth-averaged buoyancy frequency as suggested by Llewellyn Smith and Young (2002). Figs. 10 and 11 validate the use of maximum wave slope in the calculation of γ. Consequently, a ridge could become supercritical at the presence of a strong upper-ocean thermocline even when the stratification at the ridge crest is weak. The critical γ obtained in this study is about 1, independent of the ridge height. The regime of strong wave beams with $\gamma > 1.5$ is grouped in an ellipse in Fig. 12. The wave regime with $\gamma < 1$ is enclosed by a rectangle. In the latter experiments, no internal wave beams form, and internal waves of vertical modes develop over the ridge. The experiments enclosed by triangles show transition from a modal structure to wave beams.

Upward baroclinic energy flux is produced on the flank of the ridge by the tidal current. On a wide ridge ($\gamma < 1$), downward propagating waves from reflection of the surface interfere with the upward propagating waves over the ridge, producing a mode-1 standing wave. The vertical mode does not match that of free propagating waves in the undisturbed ocean; little energy propagates away from the ridge. Over a supercritical ridge ($\gamma > 1$), surface reflection of the wave beam occurs outside ridge topography. Not influenced by the upward flux on the flank of the ridge, narrow slanting wave beams form in the strongly stratified upper ocean between the surface and the base of the thermocline. The wave beams then develop into free propagating hydrostatic waves with vertical structure matching that in the undisturbed ocean. A large amount of baroclinic energy radiates away from the ridge.

The magnitude of the energy flux is proportional to HU_0^2 and the integral of N over the depths of the ridge. Over a supercritical ridge, the normalized energy reaches a constant value for ridge heights at 400 and 600 m (Fig. 12a). The local Froude number is small in these experiments (Table 2). When $F_r < 1$ and $\gamma > 1$, overturning may limit the growth of isopycnal displacement (Legg and Klymak, 2008), resulting in saturation of the energy flux for large γ. The decrease in energy flux with γ in the supercritical range for 200-m ridges in Fig. 12b is likely an artifact of lowering the ridge crest close to bottom. The small surface area of the topography reduces the total vertical flux generated on the flank of the ridge.

In an ocean with depth-varying buoyancy frequency, the WKB approximation gives the scaled ridge height

$$B = \frac{\pi \int_{-H}^{-H+h_0} N dz}{\int_{-H}^{0} N dz} = \frac{\pi h_0 \overline{N}_r}{H\overline{N}}$$

where $\overline{N} = \frac{1}{H}\int_{-H}^{0} N dz$ and $\overline{N}_r$ given by (15). In terms of B, Llewellyn Smith and Young (2003) provided a formula for energy conversion from a knife-edge ridge. In the case $f=0$, the flux is

$$F_{knife} = \rho_0 U_0^2 N_r H^2 \frac{K(B/\pi)}{\pi^2} = \rho_0 H U_0^2 \overline{N}_r h_0 \frac{\pi h_0 N_r \overline{N}_r}{4H\overline{N}^2} M(B/\pi),$$

where $M(B/\pi) = (4K(B/\pi)/\pi B^2)$. The function M for density stratification (9) is between 1 and 1.03 if the ridge height is below 600 m. The buoyancy frequency at the ridge crest is shown in Fig. 13a. After normalization by Eq. (17), the energy flux for a knife-edge ridge is $F'_{knife} = (\delta\pi N_r \overline{N}_r / 4\overline{N}^2)$, which is plotted in Fig. 13b. The flux at $h_0 = 600$ m is about half that over a supercritical bell-shaped ridge of the same height (Fig. 12a). While the normalized flux in Fig. 12a is independent of ridge height, F' calculated from the linear theory for a knife-edge ridge

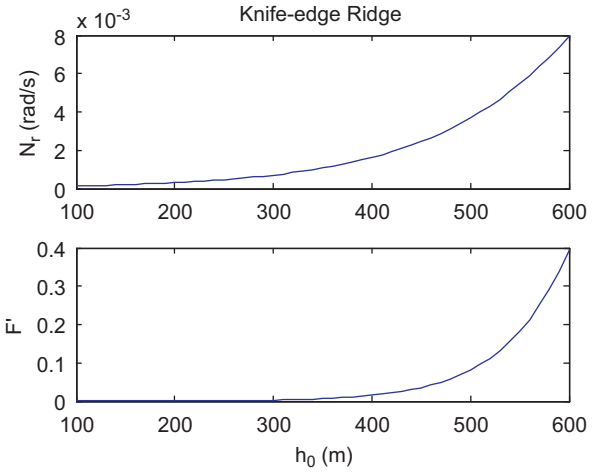

Fig. 13. (a) Buoyancy frequency at the ridge crest (N_r) from (9) as a function of the ridge height (h_0) for a knife-edge ridge with $N_0=0.015$ rad/s. (b) The normalized conversion rate (F') calculated using the formula of Llewellyn Smith and Young (2003) after normalization by (17).

is very sensitive to the ridge height. In the analytical solution, F' for a 400-m ridge is about 4% of that at 600 m. Since wave beam formation in the upper thermocline governs energy conversion in this study, it is not surprising that the normalized flux in Fig. 12a is independent of stratification at the ridge crest.

6. Summary and conclusions

Generation of internal waves by flow over bottom topography is studied using a nonhydrostatic numerical model. The numerical experiments describe the dependence of energy flux on topographic width, barotropic tidal current amplitude, and stratification at three ridge heights. The results show that the process of wave generation is governed by the ratio of the maximum topographic slope to the wave slope in the strongly stratified upper ocean. Over a subcritical ridge ($\gamma<1$), a vertical standing wave structure forms, preventing energy propagation away from a ridge. Over a supercritical ridge ($\gamma>1$), vertically propagating waves develop into slanting, narrow wave beams trapped in a wave guide between the surface and the base of the thermocline. A large amount of internal wave energy propagates away from the ridge.

Dependence of the internal wave energy flux on amplitude of the barotropic tidal current, stratification and topographic width can be summarized by a relationship between the normalized energy flux and the slope parameter in two regimes defined by the local Froude number. The energy flux is proportional to the kinetic energy of the barotropic tide in the water column and the integral of N over the depths of the ridge. The amplitude of the barotropic current does not affect the wave generation mechanism in the parameter range studied. Stratification affects energy generation in two ways. The buoyancy frequency at the ridge depths affects the vertical energy flux on the flank of the ridge. In the upper ocean, a large buoyancy frequency reduces the wave slope and increases the slope parameter. The slope parameter may become supercritical at the presence of a strong thermocline in the upper ocean.

When a ridge is supercritical but its crest is in weakly stratified water, the weakly nonlinear theory greatly underestimates the flux. Furthermore, the solution is sensitive to the ridge height (Fig. 13b). Thus, linear theory of internal wave generation cannot adequately describe the process over a tall, super-critical ridge. When the Froude number is small, a supercritical ridge produces maximum energy flux independent of the slope parameter. Since the energy flux is proportional to the stratification at depths of the ridge according to Eq. (17), only tall ridges reaching strongly stratified water contribute significantly to the energy flux in the world ocean. Furthermore, the normalized energy flux produced by a tall supercritical ridge is insensitive to ridge height and the ridge slope. Fig. 12a suggests a practical method to estimate the energy flux of internal waves in the world ocean.

In the northern South China Sea, energy of the internal wave increases during the spring tide according to Eq. (17). In addition, energy flux may become large when the Kuroshio front increases the stratification at the ridge crest in the Luzon Strait. More importantly, the slope parameter may become supercritical at the presence of a strong, shallow thermocline in the Luzon Strait. The development of a strong seasonal thermocline may explain the frequent occurrences of internal solitary waves in the northern South China Sea in spring and summer.

Acknowledgments

Suggestions provided by two reviewers help improve the manuscript. The research is supported by the Office of Naval Research of the U.S. Navy under Contracts N00014-05-1-0280 and N00014-10-1-0319.

References

Balmforth, N., Ierley, G., Young, W., 2002. Tidal conversion by subcritical topography. Journal of Physical Oceanography 32, 2900–2914.
Bell, T., 1975. Lee waves in stratified flows with simple harmonic time dependence. Journal of Fluid Mechanics 67, 705–722.
Butman, B., Alexander, P.S., Scotti, A., Beardsley, R.C., Anderson, S., 2006. Large internal waves in Massachusetts Bay transport sediment offshore. Continental Shelf Research 26 (17-18), 2029–2049.
Chao, S.-Y., Ko, D.-S., Lien, R.-C., Shaw, P.-T., 2007. Assessing the west ridge of Luzon Strait as an internal waves mediator. Journal of Oceanography 63, 897–911.
Garrett, C., Kunze, E., 2007. Internal tide generation in the deep ocean. Annual Review of Fluid Mechanics 39, 57–87.
Gerkema, T., Lam, F., Maas, L., 2004. Internal tides in the Bay of Biscay: conversion rates and seasonal effects. Deep-Sea Research II 51, 2995–3008.
Global Ocean Associates, 2004. An atlas of internal solitary-like waves and their properties. 2nd edition http://www.internalwaveatlas.com/Atlas2_index.html.
Jan, S., Lien, R.C., Ting, C.H., 2008. Numerical study of baroclinic tides in Luzon Strait. Journal of Oceanography 64, 789–802.
Khatiwala, S., 2003. Generation of internal tides in an ocean of finite depth: analytical and numerical calculations. Deep-Sea Research I 50, 3–21.
Kuo, J.E., Wang, H., Pickup, S., 1991. Multidimensional least-squares smoothing using orthogonal polynomials. Analytical Chemistry 63, 630–635.
Legg, S., Huijts, K., 2006. Preliminary simulations of internal waves and mixing generated by finite amplitude tidal flow over isolated topography. Deep-Sea Research II 53, 140–156.
Legg, S., Klymak, J., 2008. Internal hydraulic jumps and overturning generated by tidal flow over a tall steep ridge. Journal of Physical Oceanography 38, 1949–1964.
Llewellyn Smith, S., Young, W., 2002. Conversion of the barotropic tide. Journal of Physical Oceanography 32, 1554–1566.
Llewellyn Smith, S., Young, W., 2003. Tidal conversion at a very steep ridge. Journal of Fluid Mechanics 495, 175–191.
Moum, J.N., Farmer, D.M., Smyth, W.D., Armi, L., Vagle, S., 2003. Structure and generation of turbulence at interfaces strained by internal solitary waves propagating shoreward over the continental shelf. Journal of Physical Oceanography 33, 2093–2112.
Nash, J.D., Alford, M.H., Kunze, E., 2005. Estimating internal wave energy fluxes in the ocean. Journal of Atmospheric and Oceanic Technology 22, 1551–1570.
Nash, J.D., Kunze, E., Lee, C.M., Sanford, T.B., 2006. Structure of the baroclinic tide generated at Kaena Ridge, Hawaii. Journal of Physical Oceanography 36 (6), 1123–1135.
Pétrélis, F., Llewellyn Smith, S., Young, W., 2006. Tidal conversion at a submarine ridge. Journal of Physical Oceanography 36, 1053–1071.
Ramp, S.R., Tang, T.Y., Duda, T.F., Lynch, J.F., Liu, A.K., Chiu, C.-S., Bahr, F.L., Kim, H., Yang, Y., 2004. Internal solitions in the northern South China Sea. Part I: sources and deep water propagation. IEEE Journal of Oceanic Engineering 29, 1157–1181.

Ratzlaff, K.L., Johnson, J.T., 1989. Computation of two-dimensional polynomial least-squares convolution smoothing integers. Analytical Chemistry 61, 1303–1305.

Rudnick, D., Boyd, T.J., Brainard, R.E., Carter, G.S., Egbert, G.D., Gregg, M.C., Holloway, P.E., Klymak, J.M., Kunze, E., Lee, C.M., Levine, M.D., Luther, D.S., Martin, J.P., Merrifield, M.A., Moum, J.N., Nash, J.D., Pinkel, R., Rainville, L., Sanford, T.B., 2003. From tides to mixing along the Hawaiian Ridge. Science 301, 355–357.

Scotti, A., Beardsley, R.C., Butman, B., 2007. Generation and propagation of nonlinear internal waves in Massachusetts Bay. Journal of Geophysical Research 112, C10001. doi:10.1029/2007JC004313.

Shaw, P.-T., Chao, S.-Y., 2006. A nonhydrostatic primitive-equation model for studying small-scale processes: an object oriented approach. Continental Shelf Research 26, 1416–1432.

Shaw, P.-T., Ko, D., Chao, S.-Y., 2009. Internal solitary waves induced by flow over a ridge: with applications to the northern South China Sea. Journal of Geophysical Research 114, C02019. doi:10.1029/2008JC005007.

Simmons, H.L., Hallberg, R.W., Arbic, B.K., 2004. Internal wave generation in a global baroclinic tide model. Deep-Sea Research II 51, 3043–3068.

St. Laurent, L., Stringer, S., Garrett, C., Perrault-Joncas, D., 2003. The generation of internal tides at abrupt topography. Deep-Sea Research I 50, 987–1003.

Yang, Y.-J., Tang, T.Y., Chang, M.H., Liu, A.K., Hsu, M.-K., Ramp, S.R., 2004. Solitons northeast of Tung-Sha Island during the ASIAEX pilot studies. IEEE Journal of Oceanic Engineering 29, 1182–1199.

Zhao, Z., Alford, M.H., 2006. Source and propagation of internal solitary waves in the northeastern South China Sea. Journal of Geophysical Research 111, C11012. doi:10.1029/2006JC003644.